Microscopic Branching Processes: The O + O_2 Reaction and Its Relaxed Potential Representations

SERGIO RAMPINO, DIMITRIS SKOUTERIS, ANTONIO LAGANÀ

Dipartimento di Chimica, Università di Perugia, Via Elce di Sotto 8, 06123 Perugia, Italy

Received 12 January 2009; accepted 16 February 2009
Published online 26 May 2009 in Wiley InterScience (www.interscience.wiley.com).
DOI 10.1002/qua.22199

ABSTRACT: An analysis of the O_3 DMBE potential energy surface is performed using unconventional contour maps. In this way alternative paths leading to the same products (microscopic branching) are singled out. The detailed $J = 0$ quantum probabilities and related mode selectivity and energy disposal obtained through an extensive computational campaign on the EGEE production Grid are interpreted in terms of the mentioned alternative reactive paths. © 2009 Wiley Periodicals, Inc. Int J Quantum Chem 110: 358–367, 2010

Key words: oxygen exchange reaction; microscopic branching; relaxed potential representations; mode selectivity; energy disposal

1. Introduction

The O + O_2 reactive system is a study case relevant to some interesting theoretical investigations, like the understanding of the role played by insertion and abstraction processes in enhancing and/or suppressing reactivity. At the same time, the simulation of oxygen reactions is important for the control of reaction chains, like the ones involved in combustions. As to the theoretical aspects, a large amount of literature has been recently devoted to the analysis of the distinctive features of different reactive mechanisms [1–3]. In particular, potential energy surfaces (PESs) exhibiting wells, as is the PES of the title reaction [4], have been found to induce important coupling effects between different degrees of freedom and clear competition effects between reaction paths leading to the same products (microscopic branching). The phenomenon of microscopic branching, in particular, has been reported in the literature for elementary reactions [5–8]. Usually, the microscopic branching is studied by analyzing the dynamical outcome of batches of quasiclassical trajectories exploring some specific regions of the potential energy surface and therefore associable with a specific mechanism. Large batches of quasiclassical trajectories have also been

Correspondence to: S. Rampino; e-mail: ser_ram@dyn.unipg.it
Contract grant sponsor: ESA-ESTEC.
Contract grant number: 21790/08/NL/HE.
Contract grant sponsor: EGEE III.
Contract grant sponsor: COST (D37 Gridchem).

run to evaluate vibrational de-excitation and thermal rate coefficients for the exchange and dissociation reaction rates [4, 9–12] for a comparison with the available combustion experimental data (see e.g. Refs. [13, 14]).

On the contrary, despite the fact that their importance is invaluable both for the understanding of reaction mechanisms and for a more accurate evaluation of reaction rates, very little work has been reported in the literature on the calculation of exact full three-dimensional (3D) quantum detailed probabilities because of both the complexity and the heaviness of the O_3 system. Yet, quantum calculations are the only means for assessing how the structure of a complex potential energy surface affects energy disposal and microscopic branching in reactive processes which play a key role in the control of chemical processes.

To this end, we recently started investigating the title reaction by running the quantum time independent ABC program [15] on the production computing Grid segment of EGEE [16] made available to the virtual organization (VO) COMPCHEM [17], using the potential energy surface of Ref. [4]. This allowed us to calculate 3D zero total angular momentum quantum number ($J = 0$) reactive probabilities and work out the value of the thermal rate coefficient using a J-shifting model [18].

In this article the evolution of state-specific probabilities as a function of energy (excitation functions or EFs) and of state-to-state probabilities as a function of the product vibrational state (product vibrational distributions or PVDs) are analyzed in terms of microscopic branching. The attribution of some of their features to well-defined reaction paths is also attempted.

Accordingly the article is organized as follows: in Section 2 a discussion on dynamics oriented PES representations helping a qualitative analysis of the reaction mechanisms is made. In Section 3 the computational machinery associated with both the computing Grid platform and the numerical procedures used are discussed. In Section 4, the calculation and the rationalization of the $J = 0$ reactive probabilities is carried out in terms of contributions coming from different reaction paths, rotational and vibrational excitation, with the help of 2D collinear calculations using local minimum energy path-related model potentials. In the same section the disposal of energy among the internal states of the reaction products is investigated. Conclusions are drawn in Section 5.

2. The Analysis of the Potential Energy Surface

The single-valued PES function V used for the calculations is a semiempirical Double Many Body Expansion (DMBE) [19, 20] expression that has the general form

$$V = \sum_{i}^{3} V^{(2)}_{\mathrm{EHF},i} + V^{(3)}_{\mathrm{EHF}} + \sum_{i}^{3} V^{(2)}_{\mathrm{corr},i} + V^{(3)}_{\mathrm{corr}}, \quad (1)$$

made of two- ($V^{(2)}$) and three- ($V^{(3)}$) body components each partitioned into an extended-Hartree-Fock ($V^{(n)}_{\mathrm{EHF}}$) term (including the nondynamical correlation of the valence electrons in open shells or nearly degenerate orbitals) and the dynamical correlation ($V^{(n)}_{\mathrm{corr}}$) term (arising from the dynamical correlation of the electrons). Ab initio SCF potential energy values (or a function parametrized from available spectroscopic data) are used to represent $V^{(n)}_{\mathrm{EHF}}$ while $V^{(n)}_{\mathrm{corr}}$ is obtained semiempirically, by interpolation from dispersion energy coefficients of the various asymptotic channels of the potential surface. A complete description of the DMBE functional representation of the O_3 PES is given in Ref. [4].

An important first step toward the understanding of the nature of an elementary chemical reaction, and the associated energy transfer and disposal, can steam out of a graphical analysis of the related PES by both identifying its stationary points and tracing the local minimum energy paths (MEPs) interconnecting them. Unfortunately, the potential energy surface is mathematically a hypersurface in $3N - 5$ dimensions (with N being the number of atoms of the considered system) and its full dimensional representation is impossible to draw also for atom-diatom systems (as is the title one). A popular way of tackling this problem is to consider representations made of isoenergetic (equipotential) contours of the PES obtained by minimizing the potential energy along a properly selected coordinate (relaxed representations) [21, 22].

2.1. THE REDUCED SYMMETRY COORDINATE RELAXED TRIANGULAR REPRESENTATION

The authors of Ref. [4] studied the properties of the O_3 DMBE PES using the so-called relaxed triangular isoenergetic contour plots in which use was

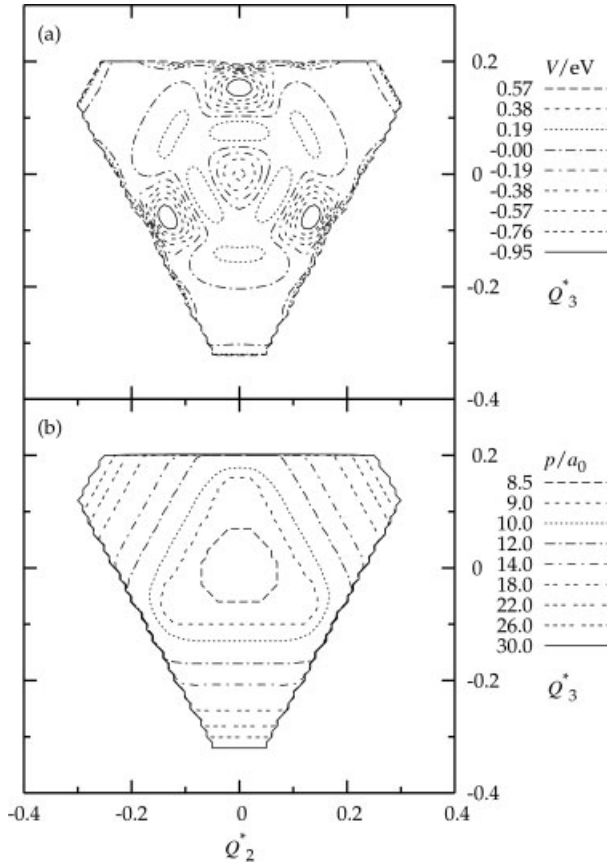

FIGURE 1. Upper panel: *p*-relaxed RS plot of the isoenergetic contours of the O_3 DMBE PES. Energy contour values are given in eV. Zero energy is taken as the O + O_2 asymptote. Lower panel: contours of the values of the relaxed perimeter given in bohr.

made of the reduced symmetry (RS) coordinates Q_2^* and Q_3^* defined as

$$Q_2^* = \frac{s_2/s_3}{\sqrt{2}} \quad Q_3^* = \frac{2s_1 - s_2 - s_3}{\sqrt{6}}, \tag{2}$$

where $s_i = r_i / \sum_{j=1}^{3} r_j$ (with $r_1 = r_{AB}$, $r_2 = r_{BC}$, $r_3 = r_{AC}$) and the relaxed variable is the perimeter (p) of the molecular triangle [23], that is the sum of the three internuclear distances.

The resulting (called *p*-relaxed RS hereinafter) plot of the isoenergetic contours of the O + O_2 system is shown in the upper panel of Figure 1. It is constructed by varying the sum of the three interatomic distances from 1 to 30 bohr. The three edge-regions correspond to the three asymptotic arrangements, while the inner sides describe reaction intermediates. The plot scans all possible reaction paths, from collinear (sides of the triangle) to perpendicular (passing through the center) atom-diatom approaches. At the sides of the triangle the resolution of the contours is too poor to allow a clear separation of possible alternative paths. When moving inwards the contours resolution improves. Worth being noted are the three equivalent C_{2v} minima associated with equilibrium O_3 structures (obtainable from each other by a rotation of 120°) and the D_{3h} minimum at $Q_2^* = Q_3^* = 0$ corresponding to a cyclic O_3. The exchange reaction going through the C_{2v} minima can follow either a longer path requiring no activation energy (as apparent by the zero energy contours drawn as dashed dotted line) or a shorter path surmounting a seemingly flat barrier region (the one crossing over the zero energy contour). The latter path can branch also into the D_{3h} minimum by surmounting a barrier of about 0.2 eV. The C_{2v}-D_{3h} isomerization requires O_3 dissociation. The corresponding relaxed p values (plotted in the lower panel of Fig. 1 as isometric contours) tell us that the perimeter of the triangle formed by the three oxygen atoms becomes increasingly smaller when following both paths. The most compact arrangement is associated with the D_{3h} geometries.

2.2. THE ARRANGEMENT HYPERSPHERICAL TREATMENT

In reactive scattering calculations widespread use is made of the hyperspherical coordinates. Isoenergetic contour plots are often drawn using the APH coordinates [24] defined as

$$\rho = \left(R_\tau^2 + r_\tau^2\right)^{1/2}, \tag{3}$$

where R_τ and r_τ are the moduli of the properly mass scaled Jacobi vectors $\mathbf{R}_\tau$ and $\mathbf{r}_\tau$ (forming an angle Θ_τ) for the generic arrangement τ, for which τ = A, B, C indicates that the isolated atom is A, B, C, respectively,

$$\theta = \tan^{-1} \frac{\left[\left(R_\tau^2 - r_\tau^2\right)^2 + (2\mathbf{R}_\tau \cdot \mathbf{r}_\tau)^2\right]^{1/2}}{2R_\tau r_\tau \sin\Theta_\tau} \tag{4}$$

and

$$2\chi_\tau = \cos^{-1} \frac{\left(R_\tau^2 - r_\tau^2\right)}{\left[\left(R_\tau^2 - r_\tau^2\right)^2 + (2\mathbf{R}_\tau \cdot \mathbf{r}_\tau)^2\right]^{1/2}} \tag{5}$$

$$2\chi_\tau = \sin^{-1} \frac{2\mathbf{R}_\tau^2 \cdot \mathbf{r}_\tau^2}{\left[\left(R_\tau^2 - r_\tau^2\right)^2 + (2\mathbf{R}_\tau \cdot \mathbf{r}_\tau)^2\right]^{1/2}}, \tag{6}$$

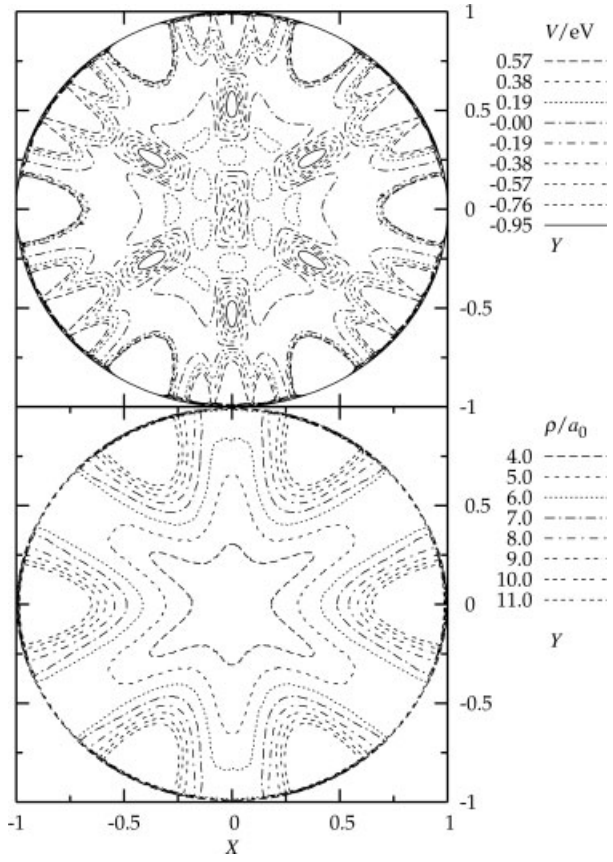

FIGURE 2. Upper panel: ρ-relaxed APH plot of the isoenergetic contours of the O_3 DMBE PES. Energy contour values are given in eV. Zero energy is taken as the O + O_2 asymptote. Lower panel: contours of the values of the relaxed hyperradius given in bohr.

in which the independent variables are the angular ones (θ and χ_τ) when the hyperradius ρ is fixed [25]. As an alternative the ρ-relaxed version [26] of these plots (called ρ-relaxed APH plots hereinafter) can be drawn by taking θ and χ_τ as independent variables and plotting their stereographic projection $X = \tan\left(\frac{1}{2}\theta\right)\cos\chi_\tau$ and $Y = \tan\left(\frac{1}{2}\theta\right)\sin\chi_\tau$ (upper panel of Fig. 2). In this kind of circular plots, the radius is a measure of θ, and the azimuthal angle χ_τ is measured from the positive X-axis. The arrangement channel A is near $\chi_\tau = 0$, while the arrangement channels B and C are, respectively, near $-2\pi/3$ and $2\pi/3$. The channels at π, $\pi/3$, and $-\pi/3$ are channels A, B, and C, respectively, after inversion. The coordinate θ represents a bending angle; $\theta = 0$ corresponds to oblate top triangular configutations, $\theta = \pi/2$ corresponds to collinear arrangements. As apparent from the upper panel of the figure interchange between opposite collinear arrangements (though not the insertion one) can occur with little energetic cost and (as suggested by the lower panel, in which the corresponding relaxed ρ values are given as isometric contours) at moderate values of the hyperradius. At half way of this insertion is possible to form the C_{2v} complex (obviously at shorter ρ values). With a little extra energy (due to a small barrier) also the D_{3h} complex can be formed and from there access all the other channels. There are clear advantages in using these plots (partially already highlighted in Ref. [25]) because they better deal with the evolution from the asymptotes of the various reaction channels.

2.3. THE PROCESS BOND ORDER HYPERSPHERICAL TREATMENT

A representation of the PES more suited to render in a simple intuitive way most of the features of the various paths connecting reactant to the product asymptotes is the one recently used in Ref. [18]. That reaction oriented picture of the PES particularly useful to discuss alternative reaction paths makes use of the so-called hyperspherical bond order (HYBO) coordinates [27, 28]. The bond order (BO) variables are defined as $n_i = \exp[\beta(r_{i\mathrm{eq}} - r_i)]$ with i = AB, BC, CA. For the A + BC $(v, j) \rightarrow$ AB (v', j') + C process (vj is the reactant vibrotational state, $v'j'$ is the product vibrotational state), the HYBO coordinates obtainable out of the BO variables are defined as

$$\rho = \sqrt{n_{\mathrm{BC}}^2 + n_{\mathrm{AB}}^2} \quad \alpha = \arctan\frac{n_{\mathrm{BC}}}{n_{\mathrm{AB}}} \tag{7}$$

and the approaching angle Φ is $\hat{\mathrm{ABC}}$. A feature of the HYBO coordinates that makes them better suited for a description of the reactive process is in fact that ρ has a clear stretching nature (one has to bear in mind here that the BO space is inverted with respect to the physical one with $n = 0$ corresponding to an infinite internuclear distance and $n = \exp[\beta r_{\mathrm{eq}}]$ corresponding to a zero internuclear distance). Another important feature is that α has the clear nature of a reaction coordinate smoothly connecting the reactant arrangement ($\alpha = 90°$) to the product one ($\alpha = 0°$).

A relaxed representation based on these coordinates makes use of Φ and η (with $\eta = \pi/4 - \alpha$) as independent variables while relaxing $\nu = 1 - \rho$ (ν can be considered as a generalized reduced symmetry variable gradually evolving from the reactant to

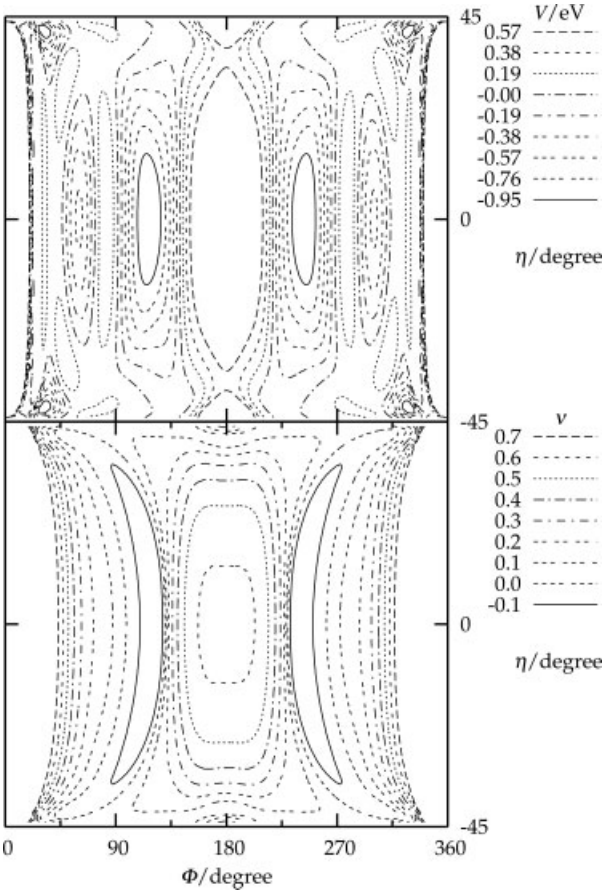

FIGURE 3. Upper panel: ν-relaxed HYBO plot of the isoenergetic contours of the O_3 DMBE PES. Energy contour values are given in eV. Zero energy is taken as the O + O_2 asymptote. Lower panel: contours of the values of the relaxed ν.

the product vibrational coordinate). This type of representation (hereinafter called ν-relaxed HYBO plot) is clearly tailored to suit a single process (the A + BC $\rightarrow$ AB + C one in our case) for which Φ varies from 180° (collinear attack of A to B on the side of B) to 360° or 0° (collinear attack of A to B on the side of C).

2.4. THE ANALYSIS OF THE O + O_2 REACTIVE PATHS USING ν-RELAXED REPRESENTATIONS

The ν-relaxed HYBO plots for the O + O_2 system obtained using the values of the BO variables ($\beta = 1.7407\ a_0^{-1}$, $r_{eq} = 2.2818\ a_0$) of Ref. [27], are shown in Figure 3 (upper panel for isoenergetic contours, lower panel for relaxed ν values contours). In the plot one can easily see that the most favored angle for reactive attacks is about 135°, in which, however, at half the way to products O_3 tends to form a stable isosceles ($\Phi \simeq 120°$) triangle [see also the lower panel of Figure 3 by bearing in mind that $\nu = 0$ corresponds to diatomic distances (at least one) near equilibrium and that as ν goes to 1 the internuclear distances tend to infinity]. Along this path as the O atom approaches the target molecule, O_2 stretches (the relaxed value of ν does not become enough negative) without giving rise to a potential energy barrier. As apparent from the figure, apart from a mild distortion of the triangular shape (a slight decrease of Φ), this path represents the most straightforward way of getting reaction. The figure shows also a second reactive path that leads to a slightly more energetic intermediate. This intermediate is equilateral and about 0.5 eV less stable than the isosceles one. A feature of this path is the double barrier structure sandwiching the well. The collinear MEP is instead highly repulsive at both $\Phi = 180°$ and $\Phi = 0°$ or 360°. The ν-relaxed HYBO plot singles out also two wells at both the top and the bottom corners. These wells are associated with the forming of a stable isosceles complex when A attacks an atom of BC diatom from the opposite extreme ($\Phi \simeq 30°$). The contour plot of the relaxed ν values also show that the attacking A atom can easily move around (relaxed ν values gradually become lower than 0) to allow isomerization to the $\Phi \simeq 120°$ C_{2v} complex.

3. The Computational Machinery

3.1. THE COMPUTING GRID DISTRIBUTION MODEL

As already mentioned, the present study was made possible by an intensive exploitation of the Grid, that is the modern paradigm of high throughput computing. A general scheme for the concurrent reorganization of the related computer programs on the Grid is the following: a distribution procedure iterates over different "events" (which consist in our case of recursive integrations of some differential equations starting from a set of given initial conditions like the initial quantum states or energies). Accordingly, the computation is articulated as a coarse grained uncoupled loop and its distributed execution model is usually called "parameter sweeping". To this end, a procedure able to handle large sets of jobs was developed. Each job execution requires the sending to the Grid of an execution script, of a specific input file and of the scattering programs. The execution script is the same for all jobs

while the input file is different for each job. To better cope with the heterogeneous nature of both the computing hardware and software (compilers, libraries, submission systems, etc.) of the Grid, executable rather than source programs were distributed over the net. In fact, despite the fact that the time required for sending the source code is considerably shorter than that required for sending its executable version (this procedure is more selective in terms of the type of machine to adopt), this approach exploits the fact that there is no need for identifying the compiler of each machine, selecting the optimal options for compilation, compiling the code, and verifying that all runs give exactly the same results as the ones obtained on the original machine.

3.2. THE QUANTUM PROBABILITIES CALCULATION

For the evaluation of quantum detailed reaction probabilities use was made of the program ABC [15], that is based on a time independent hyperspherical coordinate method. Accordingly, ABC integrates the atom-diatom Schrödinger equation for a reaction occurring on a single PES within a Born-Oppenheimer scheme for all the reactant states of a given total energy E (more details on the formalism are given in Ref. [29]). In ABC the fixed E nuclei wavefunction ψ is expanded in terms of the hyperspherical arrangement channel (τ) basis functions $B^{JM}_{\tau v_\tau j_\tau K_\tau}$ labeled after J (the total angular momentum quantum number, called `jtot`), M and K_τ (the space- and body-fixed projections of the total angular momentum $\mathbf{J}$), v_τ and j_τ (the τ asymptotic vibrational and rotational quantum numbers, with `jmax` being the maximum value of j considered in any channel), and depending on both the three Euler angles and the internal Delves hyperspherical angles. The number of basis functions has to be sufficiently large to include all the channels open at the maximum internal energy (`emax`). To carry out the fixed E propagation of the solution from small to asymptotic values of hyperradius ρ (not to be confused with the ρ of the HYBO coordinates since ρ is now defined, as is for APH coordinates, as $\rho = (R_\tau^2 + r_\tau^2)^{1/2}$) we need to integrate the equations

$$\frac{d^2\mathbf{g}(\rho)}{d\rho^2} = \mathbf{O}^{-1}\mathbf{U}\mathbf{g}(\rho). \tag{8}$$

In Eq. 8 $\mathbf{g}(\rho)$ is the matrix of the coefficients of the expansion of ψ, $\mathbf{O}$ is the overlap matrix and $\mathbf{U}$ is the coupling matrix defined as

$$U^{\tau' v'_\tau j'_\tau K'_\tau}_{\tau v_\tau j_\tau K_\tau} = \left\langle B^{JM}_{\tau v_\tau j_\tau K_\tau} \left| \frac{2\mu}{\hbar^2}(\bar{H} - E) - \frac{1}{4\rho^2} \right| B^{JM}_{\tau' v'_\tau j'_\tau K'_\tau} \right\rangle, \tag{9}$$

with μ being the reduced mass of the system and $\bar{H}$ the set of terms of the Hamiltonian operator not containing derivatives with respect to ρ. In ABC the integration of Eq. 8 is performed by segmenting the ρ interval into `mtr` ρ sectors inside each and through which the solution matrix is propagated from the ρ origin to its asymptotic value where the **S** matrix is determined [24]. The quantum **P** scattering probability matrix (whose elements are the square moduli of the state-to-state **S** matrix elements according to the relationship $P_{vj,v'j'}(E) = |S_{vj,v'j'}(E)|^2$) are then calculated for an arbitrarily fine grid of total energy values.

4. Microscopic Branching in Energy Selectivity and Disposal

4.1. A FOOTPRINT OF MICROSCOPIC BRANCHING

The excitation function calculated at $v = 0, j = 1$ is plotted in Figure 4 as a function of the translational energy E_{tr} (rather than as a function of the total energy E to better evidence threshold effects). As apparent from the figure, at $v = 0$, $j = 1$ the excitation function rises sharply already at zero translational energy as typical of processes with no barrier to reaction. Figure 4 also shows that the reactive probability first decreases and then increases again (though more slowly) as energy increases.

To characterize some features of the excitation functions which may be associated with specific paths of the PES, we carried out two-dimensional (2D) scattering calculations. For this purpose a 2D version of the RWAVEPR program was used [30] (RWAVEPR was chosen because it allows a visualization of the reactive mechanisms through the plot of screenshots of the time evolution of the wavepacket) and of the corresponding local minimum-energy reaction-path 2D cuts of the potential (since these mimick the MEP of the considered microprocess). In particular, a no-barrier energy profile going through the C_{2v} minimum (and constructed by relaxing ν in an interval of Φ ranging from 115° to 145°) and a double barrier (sandwiching a well) energy profile going through the D_{3h} minimum (and constructed by relaxing ν in an interval of Φ ranging from 60° to 90°) were considered.

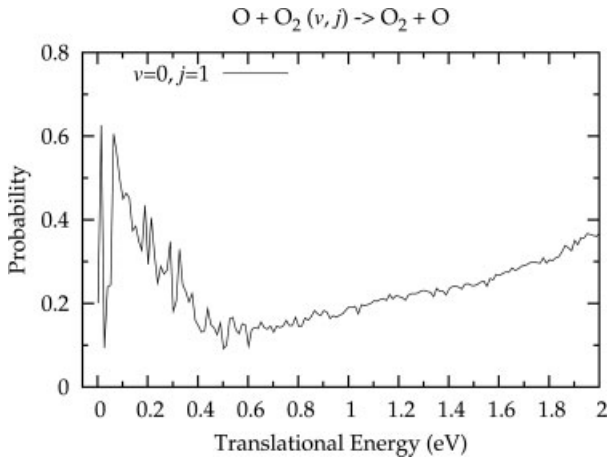

FIGURE 4. State-specific reaction probability plotted as a function of translational energy (energy spacing 0.0125 eV) for $v = 0, j = 1$ ($E_{vj} = 0.09786$ eV).

The excitation functions calculated at $v = 0$ for the 2D attractive and the (double) barrier model potentials are plotted against translational energy in Figure 5 as solid and dashed line, respectively. For the no barrier case the excitation function rises sharply at threshold and has a strongly resonant, though on the average constant, value. On the contrary, for the barrier case, the excitation function has a threshold of about 0.16 eV that reasonably well compares with the height of the saddle shown in the upper panel of Figure 3.

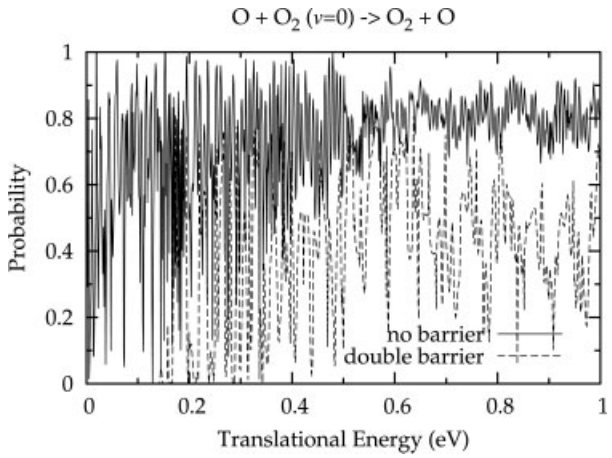

FIGURE 5. State-specific reaction probability calculated on the 2D model potentials at $v = 0$ plotted as a function of translational energy (energy spacing 0.001 eV). Solid line: no barrier model potential; dashed line: double barrier sandwiching the D_{3h} well model potential.

This suggests that the full 3D results plotted in Figure 4 may be understood in terms of a reactivity conveyed already at low energy through a no barrier reactive channel plus, as energy increases, a contribution associated with the overcoming of a barrier.

4.2. MODE SELECTIVITY

An increase of the vibrational excitation of the reactant molecule from $v = 0$ to $v = 1$ (while keeping the rotational state $j = 1$ unchanged) makes the reactive probability (averaged over local fluctuations) to be 0.1 larger than that of the ground vibrational state, as shown in Figure 6 by the plot of the difference between the excitation function calculated at $v = 0$ and $j = 1$ and the one calculated at $v = 1$ and $j = 1$. This means that the corresponding reactant vibrational energy surplus promotes (by a constant amount) the reactive probability by funneling laterally (smaller values for $\Phi < 180°$) a larger fraction of the wavepacket flux over the barrier.

Rotational excitation of the reactant O_2 to $j = 29$ (that is comparable in energy with the vibrational excitation to $v = 1$) at low energy reduces the reactivity by subtracting flux along the MEP significantly altering so far the dependence of the reactive probability on the collision energy (see dashed line of Fig. 6). As apparent from the figure, where the difference between the excitation function calculated at $v = 0$ and $j = 1$ and the one calculated at $v = 0$

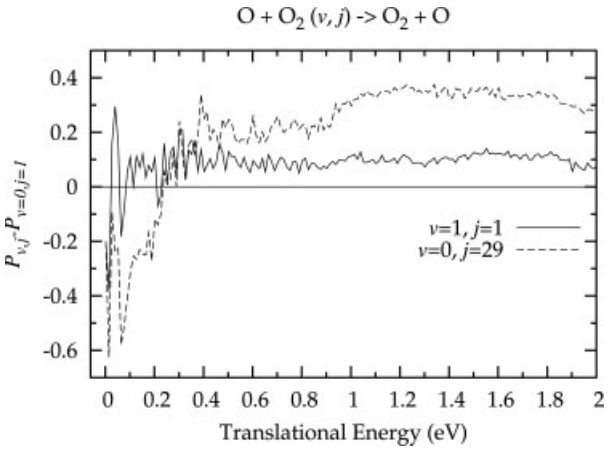

FIGURE 6. Difference of the state-specific reaction probability calculated at *vj* from the one calculatet at $v = 0, j = 1$ plotted as a function of translational energy (energy spacing 0.0125 eV). Solid line: $v = 1, j = 1$ ($E_{vj} = 0.29026$ eV); dashed line: $v = 0, j = 29$ ($E_{vj} = 0.25219$ eV).

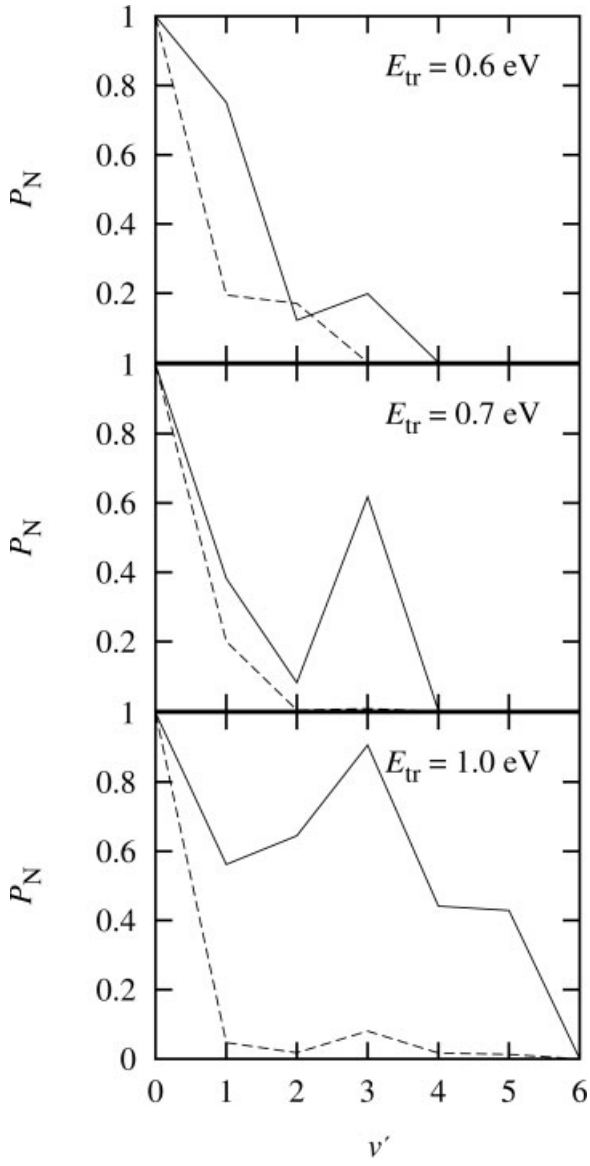

FIGURE 7. State (v) to state (v') probabilities calculated at $v = 0$ on both the no barrier (solid line) and double barrier (dashed line) model potentials plotted as a function of v' and normalized to the maximum.

and $j = 29$, when increasing j the sharp increase at zero translational energy has almost disappeared (a kind of residual footprint of this structure survives as a broad bump around 0.4 eV) while the overall shape is typically that of reactive processes occurring through the overtaking of a barrier. This is due to the fact that a rotational excitation displaces the wavepacket out of the MEP where the interaction time becomes too short and disposes it on alternative paths.

4.3. PRODUCT VIBRATIONAL ENERGY DISTRIBUTIONS

Another footprint of the competition between the different reaction paths can be found also in product vibrational distributions (PVDs). In Figure 7, the 2D barrier (dashed line) and no barrier (solid line) model probabilities calculated at $v = 0$ and normalized to the maximum (P_N) are plotted. The various PVDs are plotted as a function of the v' product vibrational quantum number at $E_{tr} = 0.6, 0.7$, and 1.0 eV for the two model potentials. A key feature of the no barrier PVDs appears to be the larger width of the distribution and its structured shape. The calculated PVDs show, in fact, a secondary peak at quite high v' values that may compete in height with the adiabatic-like one while the barrier ones have a clearer adiabatic-like nature.

When such an analysis is performed on 3D results (see Fig. 8 in which a pseudo tridimensional plot of the PVDs is given as a function of translational energy), the contribution of the no barrier path is visually identifiable as the higher maximum moving to higher v' as E_{tr} increases. The amplitude of the higher v' maximum decreases with energy to vanish at about $E_{tr} = 1.2$ eV in agreement with the results obtained for the excitation function.

4.4. MULTIQUANTUM VIBRATIONAL EXCITATION AND DE-EXCITATION

As just discussed, the reaction taking place at $v = 0, j = 1$ tends to have a peak about the highest energetically allowed vibrational state while keeping at low v' values the adiabaticity peak ($v' = v =$

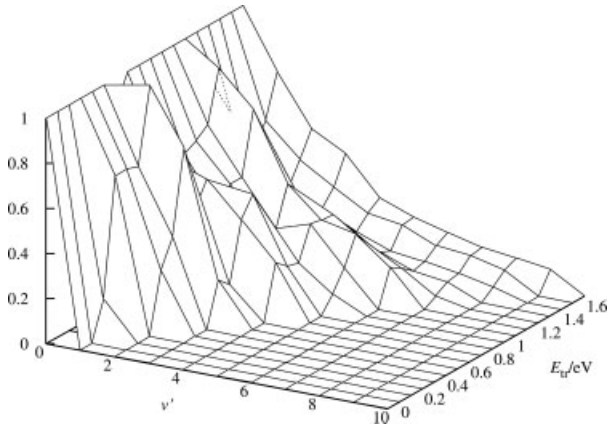

FIGURE 8. Normalized to the maximum PVDs plotted as a function of the collision energy.

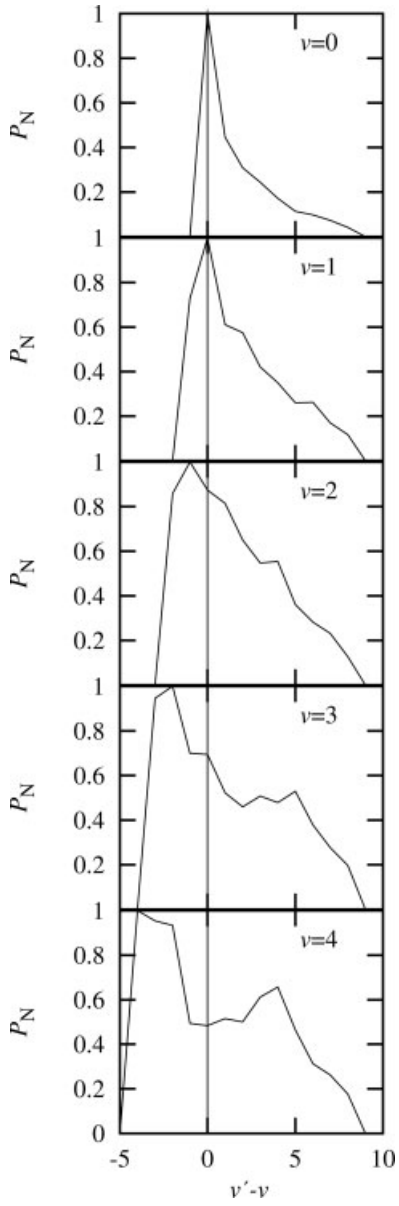

FIGURE 9. Vibrational displacement distributions calculated at $E_{tr} = 1.5$ eV, $j = 1$, and $v = 0, 1, 2, 3, 4$ (from the top to the lower panel, respectively).

0). However, we found it interesting to investigate whether this occurs because of a real vibrotational adiabaticity of the process or because of the special limiting situation of the ground state. To this end we analyzed the internal energy redistribution taking place for reactive exchanges at a fixed translational energy of 1.5 eV and several rovibrational reactant states. Normalized to the maximum PVDs evaluated at $j = 1$ and different v values are shown in Figure 9 as a function of the Δv (v' and v quantum numbers difference). As apparent from the figure, by vibrationally exciting the reactant molecule the process gains increasing diabaticity (that not necessarily implies a large energy disposal to lower states). Actually, despite the fact that for $v > 1$ de-excitation to a lower excited vibrational state becomes the most likely event, there is also a strong propensity to significantly populate vibrationally excited levels of the products. This clearly disproves all those model kinetic treatments assuming single quantum vibrational de-excitation to be the most likely process to occur and multiquantum jumps to result only via cascade mechanisms [31].

The importance of multiquantum de-excitation was already pointed out in the past [11] to be a distinctive feature of reactions occurring on PESs presenting potential wells. Specific of present quantum results is the fact that while confirming multiquantum de-excitations they also point out the important contribution of multiquantum excitation.

5. Conclusions

The detailed investigation of the state-specific and state-to-state reactive probabilities for the fairly heavy $O + O_2$ system was carried out using exact quantum means based on full 3D and reduced 2D dimensionality approaches. To this end extended calculations on the segment of the EGEE Grid available to the COMPCHEM VO were carried out and the excitation functions calculated at different compositions of the amount of energies allocated to the various internal degrees of freedom. The key rationale for understanding the results was provided by the microscopic branching of the reaction along different reaction paths singled out in plots of the interaction drawn using hyperspherical bond order coordinates contour maps. The competition between two alternative reaction paths leading to opposite behaviors at low and high collision energy was in fact spotted in the main features of the calculated excitation functions and product internal energy distributions after a comparison with 2D-path model calculations. In particular, it was found that while the addition of further vibrational energy almost evenly increases the reaction probability at all values of collision energies an increase of rotational energy has first a depressing effect on the excitation function that when energy increases is not only eliminated, but reactivity is significantly enhanced. Microscopic branching characterizes also product distributions which bear the characteristics of populating both

high and low vibrational energy product state on a quite wide range. The most striking consequence of this is the fact that multiquantum jumps are found to occur for both de-excitation and excitation.

References

1. Levine, R. D.; Bernstein, R. B. Molecular Reaction Dynamics and Chemical Reactivity; Oxford University Press: New York, 1972.
2. Laganà, A.; Lendvay, G., Eds. Theory of Chemical Reaction Dynamics; Kluwer Academic: Dordrecht, 2004.
3. Liu, X.; Lin, J. J.; Harich, S.; Schatz, G. C.; Yang, X. Science 2000, 289, 1536.
4. Varandas, A. J. C.; Pais, A. A. C. C. Mol Phys 1988, 65, 843.
5. Polanyi, J. C.; Schreiber, J. L.; Skrlac, W. J. Faraday Discuss Chem Soc 1979, 67, 66.
6. Alvariño, J. M.; Laganà, A. Chem Phys Lett 1990, 168, 448.
7. Alvariño, J. M.; Laganà, A. J Chem Phys 1991, 95, 998.
8. Alvariño, J. M.; Rodríguez, A.; Laganà, A.; Hernández, M. L. Chem Phys Lett 1999, 313, 299.
9. Pais, A. A. C. C.; Varandas, A. J. C. J Mol Struct (TEOCHEM) 1988, 166, 335.
10. Laganà, A.; Riganelli, A.; Ochoa de Aspuru, G.; Garcia, E.; Martinez, M. T. In Molecular Physics and Hypersonic Flows; Capitelli, M., Ed.; Kluwer Academic: Dordrecht, 1996; p 35.
11. Laganà, A.; Riganelli, A.; Ochoa de Aspuru, G.; Garcia, E.; Martinez, M. T. Chem Phys Lett 1998, 288, 616.
12. Esposito, F.; Armenise, I.; Capitta, G.; Capitelli, M. Chem Phys 2008, 351, 91.
13. Croce de Cobos, A. E.; Troe, J Int J Chem Kinet 1984, 16, 1519.
14. Andersen, S. M.; Klein, F. S.; Kaufman, F. J Chem Phys 1985, 83, 1648.
15. Skouteris, D.; Castillo, J. F.; Manolopoulos, D. E. Comp Phys Commun 2000, 133, 128.
16. Enabling Grids for E-Science in Europe. Available at: http://eu-egee.org (accessed on October 22, 2008).
17. Laganà, A.; Riganelli, A.; Gervasi, O. Lecture Notes Comp Sci 2006, 3980, 665.
18. Rampino, S.; Skouteris, D.; Laganà, A. Theor Chem Acc. DOI: 10.1007/s00214-009-0524-1.
19. Varandas, A. J. C. Mol Phys 1984, 53, 1303.
20. Pastrana, M. R.; Quintales, L. A. M.; Brandao, J.; Varandas, A. J. C. J Phys Chem 1990, 94, 8073.
21. Laganà, A. Comput Chem 1980, 4, 137.
22. Murrell, J. N.; Sorbie, K. S.; Varandas, A. J. C. Mol Phys 1976, 32, 1359.
23. Varandas, A. J. C. Chem Phys Lett 1987, 138, 455.
24. Pack, R. T.; Parker, G. A. J Chem Phys 1987, 87, 3888.
25. Aquilanti, V.; Laganà, A.; Levine, R. D. Chem Phys Lett 1989, 158, 87.
26. Parker, G. A.; Laganà, A.; Crocchianti, S.; Pack, R. T. J Chem Phys 1995, 102, 1238.
27. Garcia, E.; Laganà, A. Mol Phys 1985, 56, 621.
28. Laganà, A.; Spatola, P.; Ochoa de Aspuru, G.; Ferraro, G.; Gervasi, O. Chem Phys Lett 1997, 267, 403.
29. Schatz, G. C. Chem Phys Lett 1988, 150, 92.
30. Skouteris, D.; Laganà, A.; Capecchi, G.; Werner, H J. Int J Quantum Chem 2004, 96, 562.
31. Capitelli, M., Ed. Non Equilibrium Vibrational Kinetics; Springer: Berlin, 1986.